



Cite this: *Phys. Chem. Chem. Phys.*, 2020, 22, 2429

# The intrinsic magnetism, quantum anomalous Hall effect and Curie temperature in 2D transition metal trihalides† **HPSTAR 907-2020**

Jiaxiang Sun,<sup>‡,ab</sup> Xin Zhong,<sup>‡,c</sup> Wenwen Cui,<sup>‡,c</sup> Jingming Shi,<sup>‡,a</sup> Jian Hao,<sup>\*a</sup> Meiling Xu<sup>‡,a</sup> and Yinwei Li<sup>‡,c</sup>

Received 15th September 2019,  
 Accepted 3rd January 2020

DOI: 10.1039/c9cp05084a

rsc.li/pccp

Searching for experimentally feasible intrinsic quantum anomalous Hall (QAH) insulators is of great significance for dissipationless electronics applications. Here we predict, based on density functional theory (DFT), that four monolayer transition metal tri-bromides (VBr<sub>3</sub>, FeBr<sub>3</sub>, NiBr<sub>3</sub>, and PdBr<sub>3</sub>) are endowed with intrinsic half-metallicity and possess quantum anomalous Hall insulating phases. DFT+*U* calculations reveal that the VBr<sub>3</sub>, NiBr<sub>3</sub>, and PdBr<sub>3</sub> monolayers undergo nontrivial to Mott insulator transitions with increasing on-site Hubbard Coulomb interaction *U* at 0.5, 2 and 3 eV. The gap opening induced by the spin-orbit coupling drives the systems into the QAH state. The Curie temperatures of the VBr<sub>3</sub>, NiBr<sub>3</sub>, and PdBr<sub>3</sub> monolayers are ~190, 100 and 110 K. Additionally, the calculated cleavage energies suggest that the free-standing VBr<sub>3</sub>, FeBr<sub>3</sub>, NiBr<sub>3</sub>, and PdBr<sub>3</sub> monolayers can be easily produced by exfoliation using adhesive tape, which may stimulate experimental research interest to achieve QAH phases.

## Introduction

The quantum anomalous Hall (QAH) effect, arising from time-reversal symmetry broken *via* internal magnetization, was first proposed by Haldane in a 2D honeycomb lattice.<sup>1</sup> Unfortunately, not much progress towards the realization of the QAH effect has been made because the host material of the 2D honeycomb-lattice was believed to be unrealistic up until graphene was successfully exfoliated in 2004.<sup>2</sup> The experimental realization of graphene not only raised the hope of achieving the QAH effect in a real 2D honeycomb-lattice system,<sup>3–5</sup> but also made the era of 2D materials come.<sup>6–8</sup>

Recently, this long-sought QAH effect has been predicted in graphene by adsorbing transition metal atoms or proximity coupling to a ferromagnetic (FM) or anti ferromagnetic (AFM) insulator,<sup>9–13</sup> and experimentally observed in V- or Cr-doped (Bi, Sb)<sub>2</sub>Te<sub>3</sub> topological insulators.<sup>14–17</sup> Realization of QAH phases is of great significance both in fundamental physics and in dissipationless electronics applications.<sup>18,19</sup>

Despite the numerous theoretical predictions and experimental studies, there are limitations for the current study of real QAH materials. The QAH phase in graphene decorated with heavy adatoms has not been realized thus far.<sup>20,21</sup> Actually, introducing long-range FM order by doping in insulating films is quite a tough task in carrying out experiments with the QAH effect.<sup>22</sup> In addition, the synthesis of such thin films based on molecular beam epitaxy is expensive and difficult to manipulate. Thus, recent efforts<sup>23–27</sup> have focused on searching for experimentally feasible intrinsic QAH insulators.

Very recent experimental discoveries of intrinsic two dimensional (2D) ferromagnetic semiconductors<sup>28,29</sup> have received much attention, not only of experimental feasibility<sup>28</sup> but also of internal ferromagnetism,<sup>25,26,30–33</sup> which might achieve the highly desirable QAH effect. It has been theoretically predicted that several 2D transition-metal tri-halides can host the QAH effect, such as RuI<sub>3</sub>,<sup>34</sup> ReX<sub>3</sub><sup>35</sup> (X = Br, I), and MnX<sub>3</sub><sup>36</sup> (X = F, Cl, Br, I). And, more importantly, 3D layered crystals with weak interlayer van der Waals interactions are easily exfoliated down to 2D monolayers.<sup>37–39</sup>

Here we studied 14 transition metal tri-bromide monolayers based on first principles calculations, and found that VBr<sub>3</sub>, FeBr<sub>3</sub>, NiBr<sub>3</sub>, and PdBr<sub>3</sub> are endowed with intrinsic half-metallicity and possess QAH insulating phases. Nontrivial states emerge of VBr<sub>3</sub>, NiBr<sub>3</sub>, and PdBr<sub>3</sub> at the Fermi level when *U* < 0.5, 2, and 3 eV. Upon further increasing the effective on-site Hubbard Coulomb interaction, they undergo a transition from the nontrivial to the Mott insulating state. The topological nontrivial properties of monolayer VBr<sub>3</sub> were identified by calculations of the Berry

<sup>a</sup> School of Physics and Electronic Engineering, Jiangsu Normal University, Xuzhou 221116, China. E-mail: jian\_hao@jsnu.edu.cn, xuml@jsnu.edu.cn

<sup>b</sup> Department of Informationization Construction and Management, Information and Network Center, Jiangsu Normal University, Xuzhou 221116, China

<sup>c</sup> Center for High Pressure Science and Technology Advanced Research, Changchun 130012, China

† Electronic supplementary information (ESI) available. See DOI: 10.1039/c9cp05084a

‡ J. S. and X. Z. contributed equally to this work.

curvature and the corresponding edge states. Besides, the Curie temperature is  $\sim 190$ , 100 and 110 K for  $VBr_3$ ,  $NiBr_3$  and  $PdBr_3$  and the Néel temperature of  $FeBr_3$  is calculated to be 70 K.

## Computational methods

Our first-principles calculations are based on density functional theory (DFT)<sup>40</sup> as implemented in the Vienna ab initio simulation package (VASP).<sup>41</sup> The external potential is given by the projector augmented-wave (PAW) approximation,<sup>42</sup> and the exchange–correlation functional is given by the generalized gradient approximation parameterized by Perdew, Burke, and Ernzerhof (GGA-PBE).<sup>43</sup> The electron–ion interaction was described by projector augmented-wave potentials, with  $4p^63d^44s^1$  and  $4s^24p^5$  configurations treated as the valence electrons of V and Br, respectively. The plane-wave cutoff energy is set to be 500 eV in all first-principles calculations, and the first Brillouin zone is sampled using a  $\Gamma$ -centered ( $11 \times 11 \times 1$ ) Monkhorst–Pack grid.<sup>44</sup> The convergence criteria for energy and the ionic force were set to  $10^{-5}$  eV and  $0.01$  eV  $\text{\AA}^{-1}$ , respectively. Sufficient vacuum was used along the  $z$  direction, *i.e.* perpendicular to the 2D sheet, to avoid spurious interaction among the periodic images. SOC was included in the self-consistent calculations. The effective Hubbard  $U$  term is considered to address the self-interaction error of the generalized gradient approximation.<sup>45</sup> The dynamic stability of monolayer  $VBr_3$  was verified by phonon dispersion analyses through the direct supercell method, as implemented in the PHONOPY code. Ab initio molecular dynamics (AIMD) simulations were performed with the Nosé–Hoover thermostat to confirm the thermal stability. Based on the Wannier functions<sup>46</sup> obtained from the first-principles calculations, we constructed the edge Green's function of the semi-infinite  $VBr_3$  monolayer. The Berry curvature was calculated by Wannier interpolation. In order to integrate the Berry curvature, a much denser  $k$  mesh of ( $120 \times 120 \times 1$ ) was adopted.

## Results and discussions

### A. Structure and electronic structures of monolayer transition metal tri-bromides

In reality, transition metal tri-halides  $MX_3$  ( $M$  is a metal cation and  $X$  is a halogen anion) have been reported to adopt either the monoclinic  $AlCl_3$  structure type or the rhombohedral  $BiI_3$  structure type,<sup>47</sup> as illustrated in Fig. 1. The monolayer structure of transition metal tri-bromides is composed of a honeycomb net of  $M$  metal cations that are in edge sharing octahedral coordination, derived from the bulk. In the octahedral coordination environments of the  $M$  atoms, the electronic and magnetic properties can be tuned by their electron configuration. The electronic structures of the transition metal tri-bromides we considered in this study using the PBE functional are shown in Fig. S1 and S2 (ESI<sup>†</sup>). We can find that (1) most of the transition metal tri-bromides are ferromagnetic except nonmagnetic  $CoBr_3$  and  $RhBr_3$ ; (2) most of the ferromagnetic materials are half-metallic except semiconductors  $CrBr_3$  and  $MoBr_3$ ; (3) most of

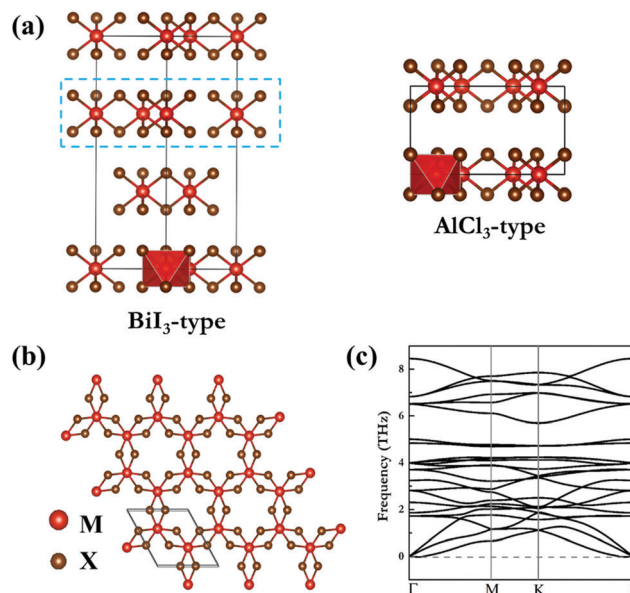


Fig. 1 A side view of (a) the  $BiI_3$  and  $AlCl_3$  structure types and (b) a plan view of common monolayers with coordinate systems corresponding to each structure type. (c) The phonon band structure of monolayer  $VBr_3$ .

the half-metallic materials can host a Dirac point except  $ZrBr_3$ ; and (4) the spin-polarized massless Dirac fermions of  $VBr_3$ ,  $FeBr_3$ ,  $NiBr_3$  and  $PdBr_3$  are found at the high-symmetry  $K$  point of the Brillouin zone. Then, we focus on further analyzing the structural characteristics, and electronic and magnetic properties of  $VBr_3$ ,  $FeBr_3$ ,  $NiBr_3$  and  $PdBr_3$ .

### B. Structure and stability

The optimized structures of the  $MBr_3$  ( $M = V, Fe, Ni, \text{ and } Pd$ ) monolayers are composed of a  $Br-M-Br$  sandwich where a sheet of  $M$  atoms is sandwiched between two sheets of  $Br$  atoms. The unit cell is composed of two  $M$  atoms and six  $Br$  atoms, and  $M$  is in octahedral coordination with  $Br$  atoms. The corresponding lattice constants and bond lengths of  $VBr_3$ ,  $FeBr_3$ ,  $NiBr_3$  and  $PdBr_3$  are listed in Table 1. We have studied the lattice dynamics adopting ( $3 \times 3$ ) supercells by calculating the phonon dispersions. As presented in Fig. 1c, the absence of imaginary modes in the entire Brillouin zone confirms that monolayer  $VBr_3$  is dynamically stable. Note that the  $FeBr_3$ ,  $NiBr_3$ , and  $PdBr_3$  monolayers are also dynamically stable.<sup>48–50</sup> After heating at room temperature (300 K) with a time step of 1 fs, no structure reconstruction is found to occur, indicating that they are also thermodynamically stable. The snapshots of the atomic configurations of the  $VBr_3$ ,

Table 1 The optimized lattice constants ( $a$ ,  $\text{\AA}$ ) and bond lengths ( $d$ ,  $\text{\AA}$ ), and thickness ( $h$ ,  $\text{\AA}$ ) of  $VBr_3$ ,  $FeBr_3$ ,  $NiBr_3$  and  $PdBr_3$  at the PBE level. The “thickness” of this monolayer is defined as the distance between the vertical coordinates of the top- $Br$  layer and the bottom- $Br$  layer

Compounds	$a$	$d_{Br-M}$	$h$
$VBr_3$	6.61	2.54	2.92
$FeBr_3$	6.36	2.45	2.80
$NiBr_3$	6.30	2.45	2.81
$PdBr_3$	6.67	2.57	2.87

FeBr<sub>3</sub>, NiBr<sub>3</sub>, and PdBr<sub>3</sub> monolayers at the end of the AIMD simulations are shown in Fig. S3 (ESI<sup>†</sup>). Moreover, we have performed a first-principles swarm structural search<sup>51,52</sup> and found that the structure in Fig. 1(b) is the global minimum.

### C. Experimental feasibility

The weak van der Waals interaction in the layered bulk crystals allows monolayer transition metal tri-bromides to be obtained from the crystal using mechanical exfoliation. To obtain a free-standing membrane, the cleavage energy needed to be overcome in the exfoliation process should be small. A large gap  $d$  between two layers representing a fracture in the bulk is introduced to simulate the exfoliation procedure. The cleavage energies as a function of  $d$  calculated using the optB86b-vdW functional are shown in Fig. 2. It can be seen that the cleavage energies for the VBr<sub>3</sub>, FeBr<sub>3</sub>, NiBr<sub>3</sub>, and PdBr<sub>3</sub> materials are 0.28, 0.12, 0.14, and 0.17 J m<sup>-2</sup>, significantly smaller than that of MoS<sub>2</sub> (0.27 J m<sup>-2</sup>) and graphite (0.37 J m<sup>-2</sup>).<sup>53</sup> Thus, free-standing VBr<sub>3</sub>, FeBr<sub>3</sub>, NiBr<sub>3</sub>, and PdBr<sub>3</sub> monolayers can be easily produced by exfoliation using adhesive tape.

### D. Electronic properties and Curie temperature

The values of the M–Br–M angles for VBr<sub>3</sub>, FeBr<sub>3</sub>, NiBr<sub>3</sub>, and PdBr<sub>3</sub> are 97.42°, 95.89°, 95.90° and 97.00°. According to the Goodenough–Kanamori–Anderson (GKA) rules the superexchange interaction of a 90° cation–anion–cation angle favors FM ordering whereas a 180° angle favors antiferromagnetic.<sup>54,55</sup> Thus, the superexchange interactions between two nearest-neighbor M atoms mediated by Br are expected to be dominant leading to an FM ground state. We consider four possible magnetic configurations (one FM and three AFM) to determine the optimal magnetic coupling, as shown in Fig. S4 (ESI<sup>†</sup>), and calculate the energy difference between the ferromagnetic and antiferromagnetic states, listed in Table S1 (ESI<sup>†</sup>). The FM states in VBr<sub>3</sub>, NiBr<sub>3</sub> and PdBr<sub>3</sub> have the lowest total energy and an AFM state in FeBr<sub>3</sub> has the lowest total energy. One of the important

properties of ferromagnets and antiferromagnets is the Curie temperature and Néel temperature. Using Monte Carlo (MC) simulations based on the 2D Ising model, we have calculated the Curie temperature of VBr<sub>3</sub>, NiBr<sub>3</sub> and PdBr<sub>3</sub> and the Néel temperature of FeBr<sub>3</sub>. For simplicity, only the nearest neighbor (NN) exchange interaction is considered since the second and third NN exchange interactions are smaller than the first NN exchange interactions.<sup>36</sup> The NN exchange-coupling parameters  $J$  can be extracted by mapping the total energies of the systems with different magnetic structures to the Ising model:

$$H = - \sum_{ij} JS_i \cdot S_j$$

where  $S$  is the net magnetic moment at the M site, and  $i$  and  $j$  represent the nearest M atoms. By comparing the total energies of ferromagnetic and antiferromagnetic states ( $E_{\text{ex}}$ ), the exchange parameter can be evaluated by  $J = E_{\text{ex}}/6S^2$ ; we obtain  $J = 9.2, 19$  and  $20$  meV for VBr<sub>3</sub>, NiBr<sub>3</sub> and PdBr<sub>3</sub>. For FeBr<sub>3</sub>, the exchange parameter is  $-13$  meV. A positive/negative value represents FM/AFM coupling. The calculated Curie temperature is  $\sim 190, 100$  and  $110$  K (Fig. 3) for VBr<sub>3</sub>, NiBr<sub>3</sub> and PdBr<sub>3</sub>, which is comparable with that of other 2D FM materials.<sup>35,56,57</sup> The Néel temperature is calculated to be 70 K.

It is widely accepted that the magnetocrystalline anisotropic energy (MAE) closely correlates with the thermal stability of magnetic data storage of a magnetic material. In general, the larger the MAE, the better the performance for data storage. Here, two magnetization directions in plane, that is the [110] and [1–10] directions, and one direction out of plane, that is the [001] direction, are considered, as summarized in Table S2 (ESI<sup>†</sup>). Among them, the in-plane [110], [1–10], and [110] directions for VBr<sub>3</sub>, NiBr<sub>3</sub> and PdBr<sub>3</sub> are the easy axis, respectively.

The band structure of the FM ground state for the VBr<sub>3</sub> monolayer is shown in Fig. 4(a). VBr<sub>3</sub> can be approximately characterized as a “zero-gap half-metal” in the case without

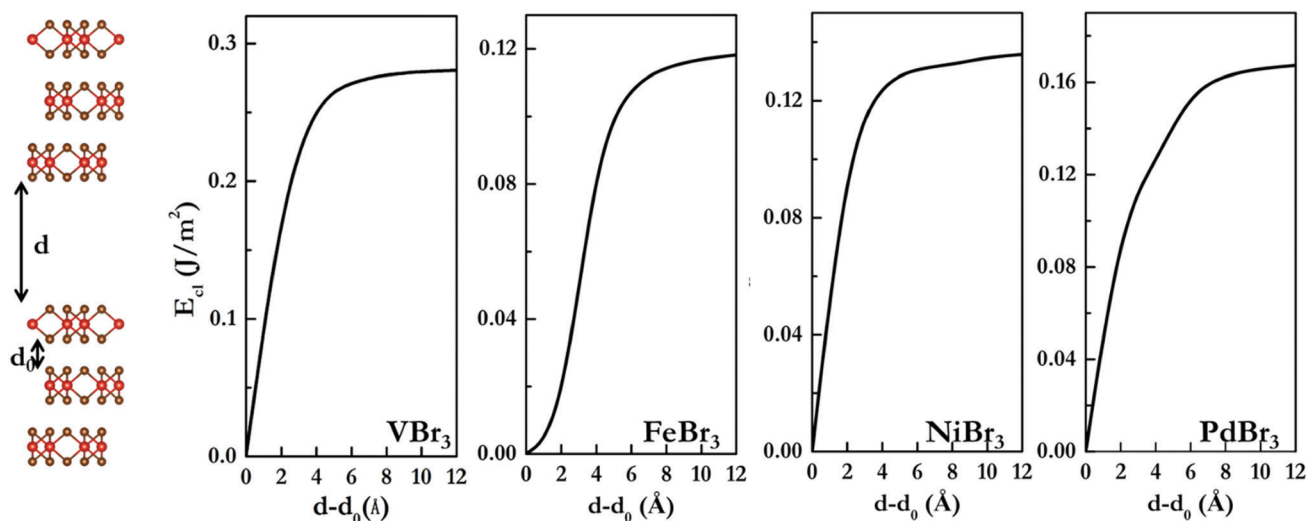


Fig. 2 Supercell model used to simulate the exfoliation procedure and the cleavage energy calculated using the optB88-vdW functional as a function of the separation  $d$  between the two fractured parts.  $d_0$  represents the equilibrium interlayer distance.

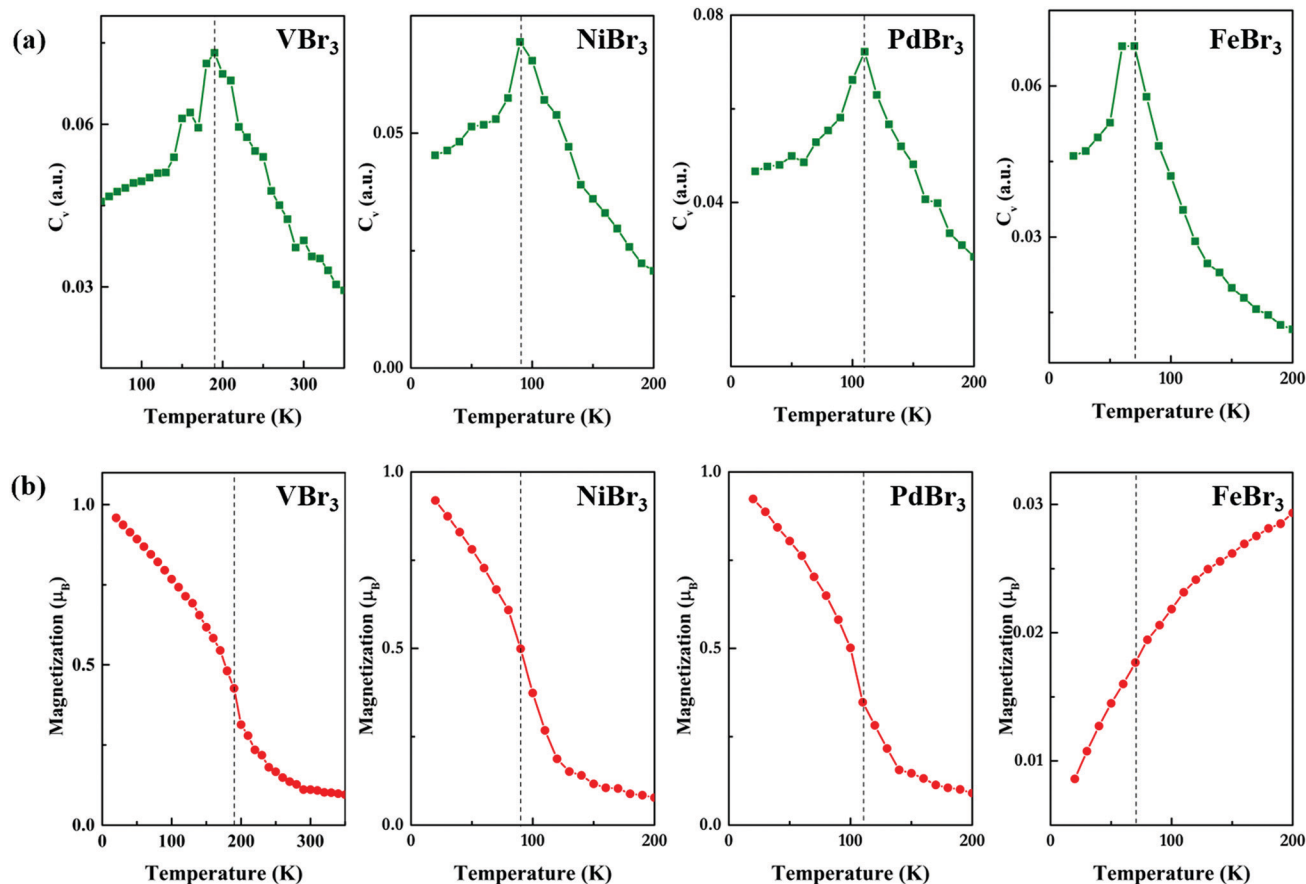


Fig. 3 Temperature variation of the heat capacity (a) and the magnetic moment (b) for the VBr<sub>3</sub>, NiBr<sub>3</sub>, PdBr<sub>3</sub> and FeBr<sub>3</sub> monolayers.

spin-orbit coupling (SOC). It has almost zero gap because of the band-toughing at the high-symmetry  $K$  point just above the Fermi level in the spin-up channel. It is nearly a half-metal because of the presence of a band gap of 2.85 eV in the spin-down channel. The Dirac states of VBr<sub>3</sub> are mainly derived from the V-d orbitals. The SOC opens a band gap of 20 meV for VBr<sub>3</sub> (Fig. 4a). Because the GGA usually underestimates the band gap, the HSE06 hybrid functional is also used to check the band gaps. Our calculations show that the band gap is 48 meV with HSE06 for the VBr<sub>3</sub> monolayer, as seen in Fig. 4b. As shown in Fig. S1 (ESI<sup>†</sup>), the FeBr<sub>3</sub>, NiBr<sub>3</sub> and PdBr<sub>3</sub> monolayers also have almost zero gaps because of the band-toughing at the high-symmetry  $K$  point. However, they are semiconducting taking the HSE functional into consideration [Fig. S5, ESI<sup>†</sup>].

The projected density of states (PDOS) and the projected band structures were calculated for the VBr<sub>3</sub> monolayer at the PBE level to gain insight into the origin of the electronic and magnetic properties (Fig. 5). Under the distorted octahedral crystal field of Br atoms, the d orbital of V would be split into one  $a_1$  orbital corresponding to the  $d_{z^2}$  orbital and two  $e_1$  and  $e_2$  orbitals corresponding to the  $(d_{xz}, d_{yz})$  and  $(d_{x^2-y^2}, d_{xy})$  orbitals. The two d electrons with spin-up lead to partially filled d orbitals, giving rise to the metal character and exhibiting a high-spin  $a_1^\uparrow e_2^\uparrow e_1^\uparrow a_1^\uparrow e_2^\uparrow e_1^\uparrow$  electronic configuration. Based on Griffith's crystal field theory, the spin states of transition

metal ions can be determined by the relative strength between crystal field splitting ( $\Delta E_{cf}$ ) and Hund exchange splitting ( $\Delta E_{ex}$ ) of d orbitals. The exchange splitting (0.96 eV) and the crystal field splitting (0.89 eV) for the VBr<sub>3</sub> monolayer lead to a high spin ( $2 \mu_B$ ) state, which is in good agreement with the V ( $a_1^\uparrow e_2^\uparrow e_1^\uparrow a_1^\uparrow e_2^\uparrow e_1^\uparrow$ ) spin configuration. The calculated magnetic moment of the V atom is  $1.97 \mu_B$  per atom, which is consistent with the  $2 \mu_B$  per atom staying in the high-spin state. Because of the hybridization with V-3d states, the Br-4p are slightly spin polarized but with an opposite moment (about  $-0.05 \mu_B$  per atom). Allowing for the delocalized feature of the Br 4p states, the FM structure between the V spins is expected to emerge in a long range.

The states near the Fermi level have main contributions from the  $a_1$  and  $e_2$  states, while the  $e_1$  state does not contribute significantly as shown in Fig. 5a. The whole occupied  $a_1$  and partially occupied  $e_2$  orbitals around the Fermi level form a Dirac point in the VBr<sub>3</sub> monolayer. The zero gap behavior in the up spin channel is the most important characteristic here, because it suggests an inverted band structure around the high symmetry  $K$  point. The V ion has a strong ferromagnetic ground state, leading to strong Zeeman splitting for energy states near the Fermi level. The presence of exchange splitting means that the band inversion of the spin-up states occurs while the spin-down energy states maintain the normal band structure.

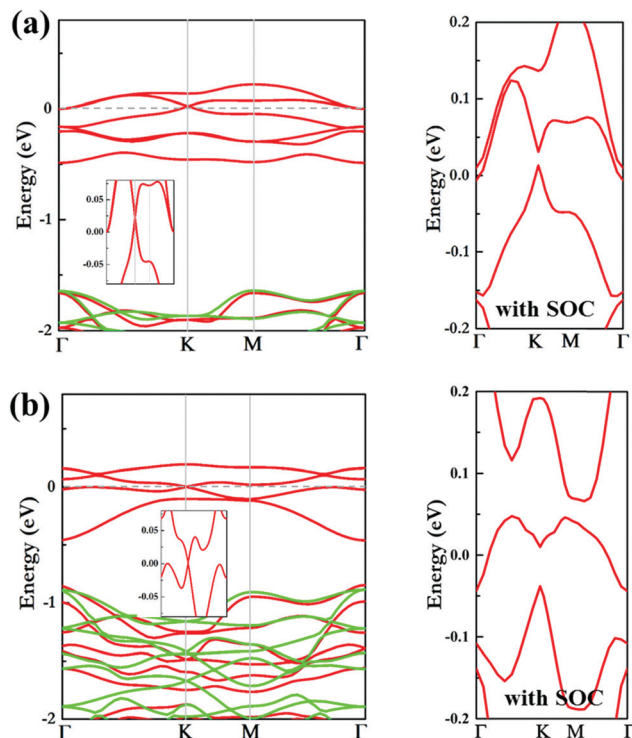


Fig. 4 Spin-polarized band structures of monolayer  $\text{VBr}_3$  without and with SOC at the (a) PBE and (b) HSE06 level. Inset: Dirac states near the Fermi level. The red and green lines represent the spin up and spin down channels, respectively.

In the down spin channel, the  $a_1$  orbital level is higher than the  $e_2$  orbital level. In sharp contrast, band inversion occurs between the  $a_1$  state and  $e_2$  orbital level in the up spin channel, as evidenced by the projected band structures in Fig. 5(b).

Next, we employ DFT+ $U$  calculations to show the effect of the on-site Coulomb repulsion  $U$  on the electronic structures of  $\text{VBr}_3$ ,  $\text{FeBr}_3$ ,  $\text{NiBr}_3$  and  $\text{PdBr}_3$  since the d electrons of a transition metal exhibit correlation effects, as shown in Fig. S6–S9 (ESI†). We can find that the  $U$  term greatly impacts the band structure of  $\text{FeBr}_3$  and as the on-site Coulomb repulsion  $U$  gradually increases, the Mott insulating phases occur at  $U$  equal to 0.5, 2 and 3 eV in the  $\text{VBr}_3$ ,  $\text{NiBr}_3$ , and  $\text{PdBr}_3$  monolayers.

### E. Quantum anomalous Hall effect

The existence of topologically protected chiral edge states is one of the most important consequences of the QAH state. To further reveal the nontrivial topological nature of the  $\text{VBr}_3$  monolayer, we calculate the edge states of the  $\text{VBr}_3$  monolayer using Green's functions based on Wannier functions obtained from PBE calculations, which reduces the cost of calculations while it does not change the topology of the electronic structure. As shown in Fig. 6, the nontrivial edge states connecting the valence and conduction bands cross the insulating gap of the Dirac cone, confirming the nontrivial topological nature of the  $\text{VBr}_3$  monolayer. The Berry curvature along the high-symmetry direction ( $\Gamma \rightarrow K \rightarrow M \rightarrow \Gamma$ ) has a sharp spike of the same sign located at the  $K$  and  $\Gamma$  points as shown in Fig. 6d. By integrating

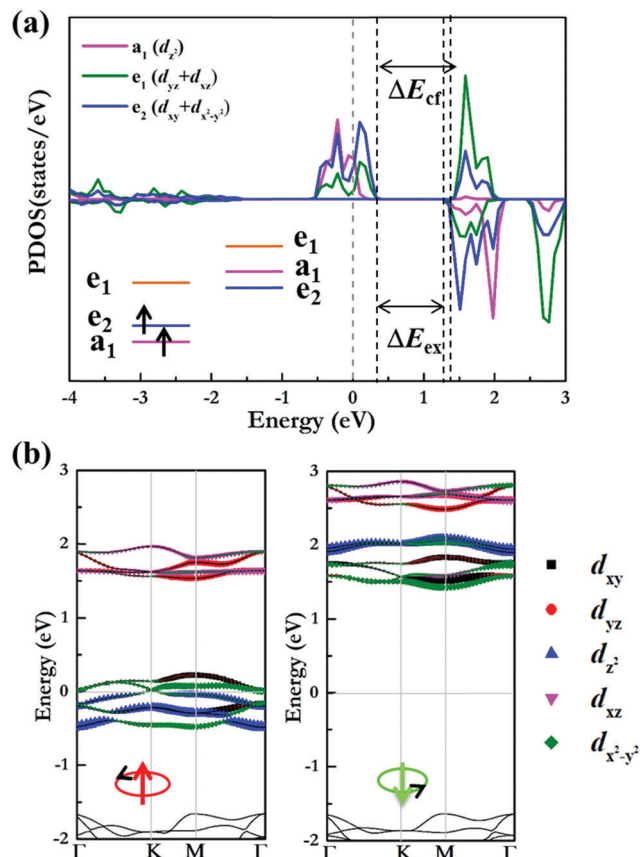


Fig. 5 (a) The PDOS of d states for V atoms is shown. (b) The projected band structures without SOC (showing the up and down spin parts separately). The relative size of each symbol indicates the V atom projection of the eigenvalue. The Fermi level is set to zero.

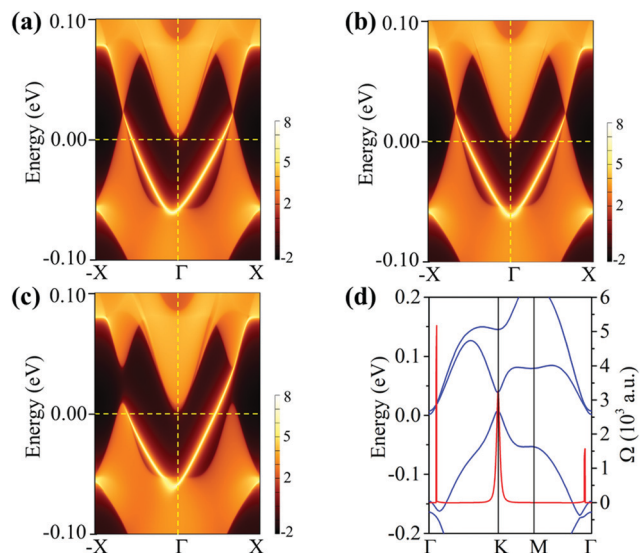


Fig. 6 The edge states and the Berry curvature of monolayer  $\text{VBr}_3$ . The V spins are in (a)  $\text{FM}^x$ , (b)  $\text{FM}^y$  and (c)  $\text{FM}^z$  configurations. (d) The distribution of the Berry curvature in momentum space for  $\text{VBr}_3$  based on the PBE method.

the Berry curvature in the entire Brillouin zone, the calculated Chern number  $C$  is  $-1$  with a non-trivial topological state. As

expected from the non-zero Chern number, the anomalous Hall conductivity shows a quantized charge Hall plateau of  $\delta_{xy} = e^2/h$  when the Fermi level is located in the insulating gap of the spin-up Dirac cone. The nontrivial topological properties of the FeBr<sub>3</sub>, NiBr<sub>3</sub> and PdBr<sub>3</sub> monolayers have been verified.<sup>32,49,50</sup>

## Conclusions

Using DFT and DFT+*U* calculations, we have performed a systematic investigation of the electronic and magnetic structures in monolayer transition metal tri-bromides, especially those of the VBr<sub>3</sub>, FeBr<sub>3</sub>, NiBr<sub>3</sub> and PdBr<sub>3</sub> monolayers. Their Dirac spin-gapless half-metallic features are characterized by a band structure with an unusually large gap in one spin channel and a Dirac cone in the other spin channel at the PBE level. Upon increasing the on-site Coulomb repulsion, the VBr<sub>3</sub>, NiBr<sub>3</sub> and PdBr<sub>3</sub> monolayers undergo a quantum phase transition from QAH insulator to Mott insulator. The calculated cleavage energies suggest that the freestanding VBr<sub>3</sub>, FeBr<sub>3</sub>, NiBr<sub>3</sub> and PdBr<sub>3</sub> monolayers can be easily obtained. Additionally, the Curie temperature is ~190, 100 and 110 K for VBr<sub>3</sub>, NiBr<sub>3</sub> and PdBr<sub>3</sub>. The Néel temperature of FeBr<sub>3</sub> is calculated to be 70 K. The combination of these unique properties renders monolayer transition metal tri-bromides a promising platform for potential applications in future spintronics.

## Conflicts of interest

The authors declare no competing financial interest.

## Acknowledgements

The authors acknowledge funding from the National Natural Science Foundation of China under Grant No. 11722433, 11904142, 11804128 and 11804129. All the calculations were performed using the High Performance Computing Center of the School of Physics and Electronic Engineering of Jiangsu Normal University.

## References

- 1 F. D. M. Haldane, Model for a Quantum Hall Effect without Landau Levels: Condensed-Matter Realization of the 'Parity Anomaly', *Phys. Rev. Lett.*, 1988, **61**, 2015–2018.
- 2 K. S. Novoselov, A. K. Geim, S. V. Morozov, D. Jiang, Y. Zhang, S. V. Dubonos, I. V. Grigorieva and A. A. Firsov, Electric Field Effect in Atomically Thin Carbon Films, *Science*, 2004, **306**, 666–669.
- 3 M. Ezawa, Spin valleytronics in silicene: Quantum spin Hall–quantum anomalous Hall insulators and single-valley semimetals, *Phys. Rev. B: Condens. Matter Mater. Phys.*, 2013, **87**, 155415.
- 4 G.-F. Zhang, Y. Li and C. Wu, Honeycomb lattice with multiorbital structure: Topological and quantum anomalous Hall insulators with large gaps, *Phys. Rev. B: Condens. Matter Mater. Phys.*, 2014, **90**, 075114.
- 5 S.-C. Wu, G. Shan and B. Yan, Prediction of Near-Room-Temperature Quantum Anomalous Hall Effect on Honeycomb Materials, *Phys. Rev. Lett.*, 2014, **113**, 256401.
- 6 S. Manzeli, D. Ovchinnikov, D. Pasquier, O. V. Yazyev and A. Kis, 2D transition metal dichalcogenides, *Nat. Rev. Mater.*, 2017, **2**, 17033.
- 7 C. Tan, X. Cao, X.-J. Wu, Q. He, J. Yang, X. Zhang, J. Chen, W. Zhao, S. Han, G.-H. Nam, M. Sindoro and H. Zhang, Recent Advances in Ultrathin Two-Dimensional Nanomaterials, *Chem. Rev.*, 2017, **117**, 6225–6331.
- 8 Y. Ren, Z. Qiao and Q. Niu, Topological Phases in Two-Dimensional Materials: A Brief Review, *Rep. Prog. Phys.*, 2016, **79**, 066501.
- 9 Z. Qiao, S. A. Yang, W. Feng, W.-K. Tse, J. Ding, Y. Yao, J. Wang and Q. Niu, Quantum anomalous Hall effect in graphene from Rashba and exchange effects, *Phys. Rev. B: Condens. Matter Mater. Phys.*, 2010, **82**, 161414.
- 10 Z. Qiao, W. Ren, H. Chen, L. Bellaïche, Z. Zhang, A. H. MacDonald and Q. Niu, Quantum Anomalous Hall Effect in Graphene Proximity Coupled to an Antiferromagnetic Insulator, *Phys. Rev. Lett.*, 2014, **112**, 116404.
- 11 J. Zhang, B. Zhao, Y. Yao and Z. Yang, Robust quantum anomalous Hall effect in graphene-based van der Waals heterostructures, *Phys. Rev. B: Condens. Matter Mater. Phys.*, 2015, **92**, 165418.
- 12 H. Zhang, C. Lazo, S. Blügel, S. Heinze and Y. Mokrousov, Electrically Tunable Quantum Anomalous Hall Effect in Graphene Decorated by 5d Transition-Metal Adatoms, *Phys. Rev. Lett.*, 2012, **108**, 056802.
- 13 J. Ding, Z. Qiao, W. Feng, Y. Yao and Q. Niu, Engineering quantum anomalous/valley Hall states in graphene via metal-atom adsorption: An ab initio study, *Phys. Rev. B: Condens. Matter Mater. Phys.*, 2011, **84**, 195444.
- 14 R. Yu, W. Zhang, H.-J. Zhang, S.-C. Zhang, X. Dai and Z. Fang, Quantized Anomalous Hall Effect in Magnetic Topological Insulators, *Science*, 2010, **329**, 61–64.
- 15 J. G. Checkelsky, R. Yoshimi, A. Tsukazaki, K. S. Takahashi, Y. Kozuka, J. Falson, M. Kawasaki and Y. Tokura, Trajectory of the anomalous Hall effect towards the quantized state in a ferromagnetic topological insulator, *Nat. Phys.*, 2014, **10**, 731–736.
- 16 X. Kou, S. T. Guo, Y. Fan, L. Pan, M. Lang, Y. Jiang, Q. Shao, T. Nie, K. Murata, J. Tang, Y. Wang, L. He, T. K. Lee, W. L. Lee and K. L. Wang, Scale-invariant quantum anomalous hall effect in magnetic topological insulators beyond the two-dimensional limit, *Phys. Rev. Lett.*, 2014, **113**, 137201.
- 17 C.-Z. Chang, W. Zhao, D. Y. Kim, H. Zhang, B. A. Assaf, D. Heiman, S.-C. Zhang, C. Liu, M. H. W. Chan and J. S. Moodera, High-precision realization of robust quantum anomalous Hall state in a hard ferromagnetic topological insulator, *Nat. Mater.*, 2015, **14**, 473–477.
- 18 J. Wu, J. Liu and X. J. Liu, Topological spin texture in a quantum anomalous hall insulator, *Phys. Rev. Lett.*, 2014, **113**, 136403.
- 19 Q. L. He, L. Pan, A. L. Stern, E. C. Burks, X. Che, G. Yin, J. Wang, B. Lian, Q. Zhou, E. S. Choi, K. Murata, X. Kou,

- Z. Chen, T. Nie, Q. Shao, Y. Fan, S. C. Zhang, K. Liu, J. Xia and K. L. Wang, Chiral Majorana fermion modes in a quantum anomalous Hall insulator–superconductor structure, *Science*, 2017, **357**, 294–299.
- 20 P.-H. Chang, M. S. Bahramy, N. Nagaosa and B. K. Nikolić, Giant Thermoelectric Effect in Graphene-Based Topological Insulators with Heavy Adatoms and Nanopores, *Nano Lett.*, 2014, **14**, 3779–3784.
- 21 A. Cresti, D. Van Tuan, D. Soriano, A. W. Cummings and S. Roche, Multiple Quantum Phases in Graphene with Enhanced Spin-Orbit Coupling: From the Quantum Spin Hall Regime to the Spin Hall Effect and a Robust Metallic State, *Phys. Rev. Lett.*, 2014, **113**, 246603.
- 22 J. Zhang, B. Zhao, T. Zhou and Z. Yang, *Chin. Phys. B*, 2016, **25**, 117308.
- 23 G. Xu, B. Lian and S.-C. Zhang, Intrinsic Quantum Anomalous Hall Effect in the Kagome Lattice  $\text{Cs}_2\text{LiMn}_3\text{F}_{12}$ , *Phys. Rev. Lett.*, 2015, **115**, 186805.
- 24 K. Dolui, S. Ray and T. Das, Intrinsic large gap quantum anomalous Hall insulators in  $\text{LaX}$  ( $X = \text{Br}, \text{Cl}, \text{I}$ ), *Phys. Rev. B: Condens. Matter Mater. Phys.*, 2015, **92**, 205133.
- 25 J. He, X. Li, P. Lyu and P. Nachtigall, Near-room-temperature Chern insulator and Dirac spin-gapless semiconductor: nickel chloride monolayer, *Nanoscale*, 2017, **9**, 2246–2252.
- 26 X.-L. Sheng and B. K. Nikolić, Monolayer of the 5d transition metal trichloride  $\text{OsCl}_3$ : A playground for two-dimensional magnetism, room-temperature quantum anomalous Hall effect, and topo, *Phys. Rev. B*, 2017, **95**, 201402.
- 27 C. Huang, J. Zhou, H. Wu, K. Deng, P. Jena and E. Kan, Quantum anomalous Hall effect in ferromagnetic transition metal halides, *Phys. Rev. B*, 2017, **95**, 045113.
- 28 B. Huang, G. Clark, E. Navarro-Moratalla, D. R. Klein, R. Cheng, K. L. Seyler, D. Zhong, E. Schmidgall, M. A. McGuire, D. H. Cobden, W. Yao, D. Xiao, P. Jarillo-Herrero and X. Xu, Layer-dependent ferromagnetism in a van der Waals crystal down to the monolayer limit, *Nature*, 2017, **546**, 270–273.
- 29 C. Gong, L. Li, Z. Li, H. Ji, A. Stern, Y. Xia, T. Cao, W. Bao, C. Wang, Y. Wang, Z. Q. Qiu, R. J. Cava, S. G. Louie, J. Xia and X. Zhang, Discovery of intrinsic ferromagnetism in two-dimensional van der Waals crystals, *Nature*, 2017, **546**, 265–269.
- 30 C. Huang, Y. Du, H. Wu, H. Xiang, K. Deng and E. Kan, Prediction of Intrinsic Ferromagnetic Ferroelectricity in a Transition-Metal Halide Monolayer, *Phys. Rev. Lett.*, 2018, **120**, 147601.
- 31 E. Torun, H. Sahin, S. K. Singh and F. M. Peeters, Stable half-metallic monolayers of  $\text{FeCl}_2$ , *Appl. Phys. Lett.*, 2015, **106**, 192404.
- 32 S.-H. Zhang and B.-G. Liu, Intrinsic 2D ferromagnetism, quantum anomalous Hall conductivity, and fully-spin-polarized edge states of  $\text{FeBr}_3$  monolayer, 2017, arXiv preprint arXiv:1706.08943.
- 33 W.-B. Zhang, Q. Qu, P. Zhu and C.-H. Lam, Robust Intrinsic Ferromagnetism and Half Semiconductivity in Stable Two-Dimensional Single-Layer Chromium Trihalides, *J. Mater. Chem. C*, 2015, **3**, 12457–12468.
- 34 C. Huang, J. Zhou, H. Wu, K. Deng, P. Jena and E. Kan, Quantum anomalous Hall effect in ferromagnetic transition metal halides, *Phys. Rev. B*, 2017, **95**, 045113.
- 35 Q. Sun and N. Kioussis, Intrinsic ferromagnetism and topological properties in two-dimensional rhenium halides, *Nanoscale*, 2019, **11**, 6101–6107.
- 36 Q. Sun and N. Kioussis, Prediction of manganese trihalides as two-dimensional Dirac half-metals, *Phys. Rev. B*, 2018, **97**, 094408.
- 37 J. Liu, Q. Sun, Y. Kawazoe and P. Jena, Exfoliating biocompatible ferromagnetic Cr-trihalide monolayers, *Phys. Chem. Chem. Phys.*, 2016, **18**, 8777–8784.
- 38 W.-B. Zhang, Q. Qu, P. Zhu and C.-H. Lam, Robust intrinsic ferromagnetism and half semiconductivity in stable two-dimensional single-layer chromium trihalides, *J. Mater. Chem. C*, 2015, **3**, 12457–12468.
- 39 N. Miao, B. Xu, L. Zhu, J. Zhou and Z. Sun, 2D Intrinsic Ferromagnets from van der Waals Antiferromagnets, *J. Am. Chem. Soc.*, 2018, **140**, 2417–2420.
- 40 W. Kohn and L. J. Sham, Self-Consistent Equations Including Exchange and Correlation Effects, *Phys. Rev.*, 1965, **140**, A1133–A1138.
- 41 G. Kresse, Ab initio molecular dynamics for liquid metals, *J. Non-Cryst. Solids*, 1995, **192–193**, 222–229.
- 42 P. E. Blöchl, Projector augmented-wave method, *Phys. Rev. B: Condens. Matter Mater. Phys.*, 1994, **50**, 17953–17979.
- 43 J. P. Perdew, K. Burke and M. Ernzerhof, Generalized Gradient Approximation Made Simple, *Phys. Rev. Lett.*, 1996, **77**, 3865–3868.
- 44 H. J. Monkhorst and J. D. Pack, Special points for Brillouin-zone integrations, *Phys. Rev. B: Solid State*, 1976, **13**, 5188–5192.
- 45 S. L. Dudarev, G. A. Botton, S. Y. Savrasov, C. J. Humphreys and A. P. Sutton, Electron-energy-loss spectra and the structural stability of nickel oxide: An LSDA+ $U$  study, *Phys. Rev. B: Condens. Matter Mater. Phys.*, 1998, **57**, 1505–1509.
- 46 A. A. Mostofi, J. R. Yates, Y.-S. Lee, I. Souza, D. Vanderbilt and N. Marzari, wannier90: A tool for obtaining maximally-localised Wannier functions, *Comput. Phys. Commun.*, 2008, **178**, 685–699.
- 47 M. McGuire, Crystal and Magnetic Structures in Layered, Transition Metal Dihalides and Trihalides, *Crystals*, 2017, **7**, 121.
- 48 P. Liu, X. Luo, Y. Cheng, X.-W. Wang, W. Wang, H. Liu, K. Cho, W.-H. Wang and F. Lu, Physical realization of 2D spin liquid state by ab initio design and strain engineering in  $\text{FeX}_3$ , *J. Phys.: Condens. Matter*, 2018, **30**, 325801.
- 49 Z. Li, B. Zhou and C. Luan, Strain-tunable magnetic anisotropy in two-dimensional Dirac half-metals: nickel trihalides, *RSC Adv.*, 2019, **9**, 35614–35623.
- 50 J.-Y. You, Z. Zhang, B. Gu and G. Su, Two-Dimensional Room-Temperature Ferromagnetic Semiconductors with Quantum Anomalous Hall Effect, *Phys. Rev. Appl.*, 2019, **12**, 024063.
- 51 Y. Wang, J. Lv, L. Zhu and Y. Ma, Crystal structure prediction via particle-swarm optimization, *Phys. Rev. B: Condens. Matter Mater. Phys.*, 2010, **82**, 094116.

- 52 Y. Wang, J. Lv, L. Zhu and Y. Ma, CALYPSO: A method for crystal structure prediction, *Comput. Phys. Commun.*, 2012, **183**, 2063–2070.
- 53 W. Wang, S. Dai, X. Li, J. Yang, D. J. Srolovitz and Q. Zheng, Measurement of the cleavage energy of graphite, *Nat. Commun.*, 2015, **6**, 7853.
- 54 P. W. Anderson, Antiferromagnetism. Theory of superexchange interaction, *Phys. Rev.*, 1950, **79**, 350–356.
- 55 J. Kanamori, Superexchange interaction and symmetry properties of electron orbitals, *J. Phys. Chem. Solids*, 1959, **10**, 87–98.
- 56 J. Liu, Q. Sun, Y. Kawazoe and P. Jena, Exfoliating biocompatible ferromagnetic Cr-trihalide monolayers, *Phys. Chem. Chem. Phys.*, 2016, **18**, 8777–8784.
- 57 P. Li, Prediction of intrinsic two dimensional ferromagnetism realized quantum anomalous Hall effect, *Phys. Chem. Chem. Phys.*, 2019, **21**, 6712–6717.